

Molecular Simulation of Oil Mixture Adsorption Character in Shale System

Shansi Tian¹, Haitao Xue^{1,*}, Shuangfang Lu¹, Fang Zeng², Qingzhong Xue³,
Guohui Chen¹, Chunzheng Wu¹, and Sansheng Zhang⁴

¹Research Institute of Unconventional Petroleum and Renewable Energy (RIUP&RE),
China University of Petroleum (East China), Qingdao, Shandong 266555, China

²School of Geosciences, China University of Petroleum, Qingdao (East China), Shandong 266555, China

³State Key Laboratory of Heavy Oil Processing, China University of Petroleum (East China), Qingdao, Shandong 266555, China

⁴PetroChina International Investment (Canada), Calgary, Alberta T2P3H9, Canada

Chemical kinetics theory and molecular dynamics simulation are used to study adsorption character of shale oil within nanoscale carbonaceous and silica slits of shale rocks. It is demonstrated that shale oil density does not remain the same throughout the pore and its oscillation attenuates from the slit surface to the central plane. In this paper, the effects of oil composition and temperature on the densities of the adsorption layers and adsorption character have been extensively examined. We find that (a) there are four adsorption layers of oil mixture on silica and graphite surface, (b) the adsorption character of single component in oil mixture depends largely on its property: the adsorption mass of high carbon number alkane increases with the numbers of adsorption layers, of which trend is contrary to that of light carbon numbers alkane; aromatic hydrocarbon has mainly one adsorption layer; the adsorption character of polar compounds depends on their electric charge, (c) silica surface is more likely to adsorb the light carbon number alkane than graphite because of its rough surface; and compounds with negative charge tend to be adsorption more on the silica surface than graphite due to the hydroxyls of silica. Graphite adsorbs more C₁₀H₈ than silica, because graphite and C₁₀H₈ have the same conjugated π bond and the shape of C₁₀H₈ is not suitable to rough surface of silica, (d) the density of adsorption layers decreases with the increase of temperature, and the effect of temperature on the adsorption of macromolecular compounds is greater. On the basis of our molecular simulation, we show the adsorption rate of shale oil on the surfaces of mineral/organic matter and the potential to assess the moveable capacity of shale oil.

Keywords: Adsorption Character, Shale Oil, Molecular Dynamics, Chemical Kinetics.

1. INTRODUCTION

With the increasing of energy demand and conventional oil and gas resources depletion, unconventional oil and gas resources are getting more and more attention, and have become a major contributor to the global oil and gas production growth. The exploration and development of shale gas has achieved a huge success in North America,^{1–3} and it leads a global shale gas research boom.^{4,5} However, with the lessons learned from shale gas and the decrease of natural gas price, the investors have shifted their attention to more profitable shale oil.^{6–8} According to the Energy Information Administration,⁹ in the last 10 years, the production of U.S. shale oil has increased 12.2 times—an average of 4.572 million barrels per day (MMbbl/d) in

2015 and 0.374 MMbbl/d in 2005. Meanwhile, driven by the exploitation of tight formations, the United States remained the world's top producer of petroleum and natural gas hydrocarbons in 2015.¹⁰ Shale oil is playing a significant role in the global energy industry, and a worldwide shale-oil boom is coming.^{11–13}

Preliminary evaluation shows that: shale oil resources are very rich in China; the amount of geological resources is 32 billion barrels. And it ranked the 3rd among the 41 countries which have a total shale oil resource of 345 billion barrels.¹⁴ At present, in China, many reserves area in which the amount of geological resources are between 5×10^8 t and 10×10^8 t have been discovered in the Triassic Yanchang Formation of Erdos Basin, Permian Lucaogou Formation of Junggar Basin, Qingshankou Formation of Songliao Basin; there are also many important

*Author to whom correspondence should be addressed.

discovery in the lime-shale of Bohai Bay area and Sichuan Basin.^{15,16} Compared with marine shale oil in the North America, the lacustrine shale oil in China more heavier and has more polar components. The amount of resin and asphaltene is much more than that in the North America. In addition, the lacustrine shale oil is easier to adsorb on the surface of the pore in the shale system and more difficult to be developed because of the polar components. The polar components should be considered in the assessment of shale oil in China. Taking into account the strong interactions between oil molecules and kerogen, minerals, together with the widespread nanopores in shale,^{17–19} the error of resource estimation caused by the ignorance of oil adsorption could not be neglected.

The adsorption of alkanes has been studied in recent years. Firstly, McGonigal et al.²⁰ directly imaged a two-dimensional, high-degree ordering of the alkane layer at the liquid/graphite interface using a scanning tunneling microscope (STM).²⁰ Castro et al.²¹ reported that longer alkane shows a strong preference for adsorption onto graphite.²¹ Furthermore, Severson and Snurr²² studied the adsorption isotherms of linear alkanes (ethane, pentane, decane, and pentadecane) on activated carbon and evaluated the functions of slit size, chain length, and temperature on adsorption.²² Harrison et al.²³ studied the single component preferential adsorption of normal and branched alkanes in slits with different apertures (1, 2, and 4 nm) at 390 K.²³ A similar issue for shale gas has been discussed by Ambrose et al.,²⁵ who suggested that an adjustment of adsorption phase volume is necessary for gas-in-place (GIP) calculations, and a 10 to 25% decrease can be obtained in comparison with the conventional method.^{24–26} In addition, Wang²⁷ reported that the unrecoverable fraction of oil-in-place (OIP) is 13% in Bakken shale,²⁷ taking the adsorption of alkane into consideration. Nevertheless, no documented study has been found that explores the effect of polar components adsorption on the shale oil-in-place estimation.

In this study, the adsorption behavior of oil mixture on shale system was studied under geological conditions using molecular dynamics (MD). Our main objectives were (1) to provide nanoscale resolution for studying the interactions at the hydrocarbon-shale interface, (2) to accurately characterize the adsorption properties of alkanes/polar compounds in the organic/mineral slit, and to provide parameters for the calculation of the unrecoverable fraction for shale OIP estimation.

2. MODELS AND METHODS

MD simulations are carried out by DISCOVER code in the MATERIAL STUDIO (MS) software developed by Accelrys Inc. The interatomic interactions are described by the force field of condensed-phase optimized molecular potential for atomistic simulation studies (COMPASS), which

is a general all-atom force field.^{28,29} It is a parameterized, tested and validated first *ab initio* force field, which enables an accurate and simultaneous prediction of various gas-phase properties and condensed-phase properties of most of common organic and inorganic materials. The MD process in this paper is firstly performed in NPT (the pressure and the temperature are constant) ensemble, and then it is performed in NVT (the temperature and the volume are constant) ensemble. The Andersen thermostat method was employed to control the system at a temperature. The van der Waals interactions are calculated by atom-based, and the cut-off distance is 15.5 Å. The electrostatic interactions are calculated by the Ewald method.

The initial silica lattice is derived from the structural database of MS software. A repeat graphite unit with the thickness 2.75 nm is cleaved along the (0 0 -1) crystallographic orientation and a repeat silica unit with the thickness 2.5 nm is cleaved along the (-1 0 0) crystallographic orientation. As known, silica surface in oil reservoir is complex and there are some other components absorbing on silica surface. In this paper, the silica surface is modified by hydroxyl groups, which is a common silica surface. And the graphite surface is represented for the kerogen surface. Methane (CH₄), ethane (C₂H₆), *n*-butane (C₄H₁₀), *n*-octane (C₈H₁₈), *n*-octadecane (C₁₈H₃₈), naphthalene (C₁₀H₈), *N,N*-dimethyldodecylamine (C₁₂H₂₅N(CH₃)₂), octadecanoic acid (CH₃(CH₂)₁₆COOH) are constructed as the oil mixture molecules in these simulations, as shown in Figures 1(a)–(h). Graphite surface is chosen as the kerogen surface and silica modified by hydroxyl groups is chosen as the mineral surface, as shown in Figures 1(i) and (j). Curtis³⁰ reported that a large number of nano scale pores appeared when R_o is higher than 0.9%.³⁰ And the pores of which size under 20 nm play an important role in the shale system.³¹ An 8 nm slit model is built to represent these pores. In preparing the configuration of the simulations, a rectangular basic box of 30.38 × 30.38 × 115.83 Å³ is built for the silica model simulations and a rectangular basic box of 29.52 × 34.09 × 114 Å³ is built for the graphite model simulations, with the *z*-axis perpendicular to the silica and graphite surfaces. Periodic boundary conditions are considered in all directions. The oil mixture molecules are packed in the silica and graphite boxes. The numbers of loading molecules in the silica and graphite models are shown in Table I. The hydrocarbon yields are calculated with the kinetics models and the kinetics parameters are used with type I kerogen,^{32,33} the evolution is shown in Figure 2. The mass fraction represents the grade of maturity at $R_o = 0.9\%$, which is a common maturity in shale oil. The methane, ethane, *n*-butane molecules are represented for the gases which are dissolved in the shale oil (C₁, C₂, C_{3–5}), the *n*-octane molecules for the low carbon numbers alkanes (C₆–C₁₄ saturated HC), *n*-octadecane molecules for the high carbon numbers alkanes (C₁₅₊ saturated HC), the naphthalene molecules for the aromatic hydrocarbons

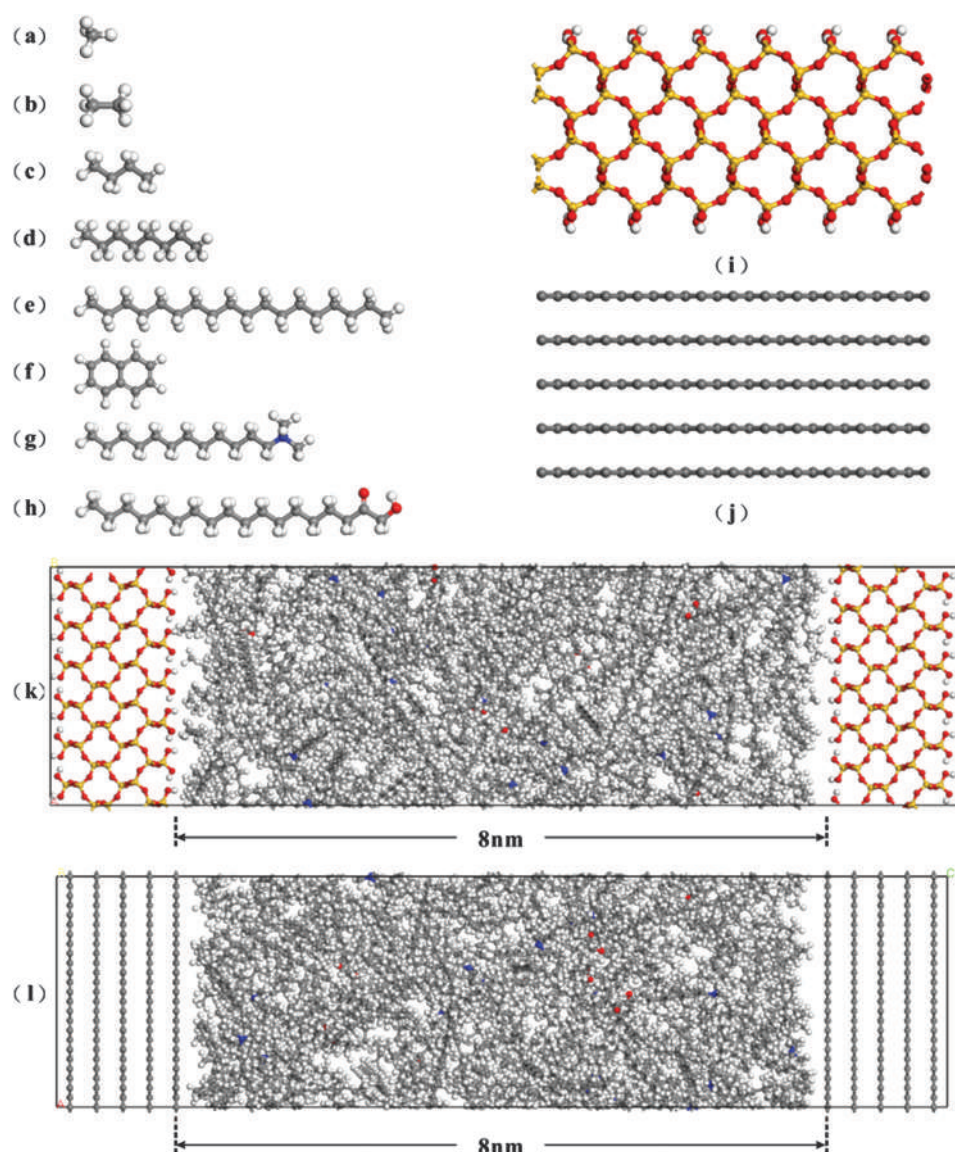


Figure 1. (a) Methane (CH_4). (b) Ethane (C_2H_6). (c) *n*-butane (C_4H_{10}). (d) *n*-octane (C_8H_{18}). (e) *n*-octadecane ($\text{C}_{18}\text{H}_{38}$). (f) naphthalene (C_{10}H_8). (g) *N,N*-dimethyldodecylamine ($\text{C}_{12}\text{H}_{25}\text{N}(\text{CH}_3)_2$). (h) octadecanoic acid ($\text{CH}_3(\text{CH}_2)_{16}\text{COOH}$). (i) Silica surface modified by hydroxyl group. (j) Graphite surface. (k) Oil mixture adsorption in the silica model. (l) Oil mixture adsorption in the graphite model. Gray, C; White, H; Red, O; Yellow, Si; Blue, N.

(C_{6+} aromatic HC), the *N,N*-dimethyldodecylamine and octadecanoic acid molecules for the polar compounds (resin and asphaltene), they are constructed in the silica and graphite boxes. The simulation models are shown in Figures 1(k) and (l). In the models, oil mixture molecules are placed in the silica and graphite slit apertures, which

are both 8 nm and represent the common nanopores in shale. All simulations are initialized by minimizing the energies of the initial configurations using the steepest decent method.³⁴ After the initialization, all the MD simulations are first carried out at an NPT ensemble which is aim to simulate the geological condition, the pressure

Table I. Mass fraction of oil mixture at $R_o = 0.9\%$ and loading molecular numbers in the silica and graphite models.

Components of shale oil	Asphaltene and resin		C_{15+} saturated hydrocarbon	C_{15+} aromatic hydrocarbon	$\text{C}_6\text{--C}_{14}$ saturated hydrocarbon	$\text{C}_3\text{--C}_5$	Ethane	Methane
Mass fraction	0.18		0.39	0.1	0.28	0.01	0.01	0.03
Chemical formula	$\text{C}_{14}\text{H}_{31}\text{N}$	$\text{C}_{18}\text{H}_{36}\text{O}_2$	$\text{C}_{18}\text{H}_{38}$	C_{10}H_8	C_8H_{18}	C_4H_{10}	C_2H_6	CH_4
Loading molecular numbers in the silica model	20	8	56	28	92	6	11	62
Loading molecular numbers in the graphite model	21	9	59	30	98	6	12	65

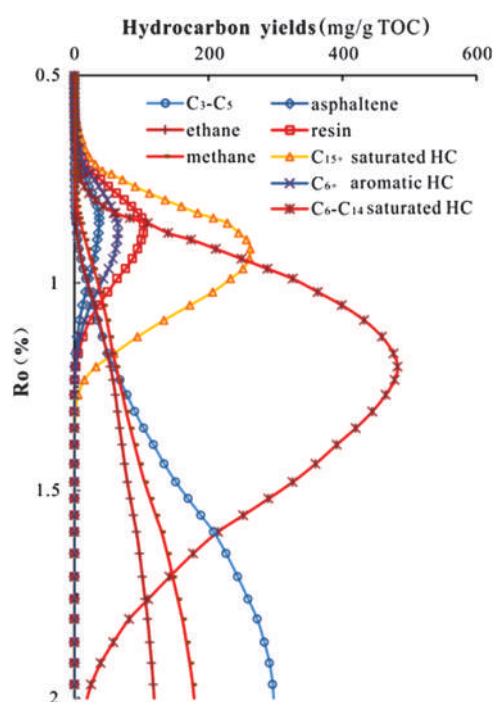


Figure 2. Evolution of type I kerogen hydrocarbon yields.

is 18 MPa and the temperature is 356 K, this condition represents the geological condition of Qing Shankou Formation in Songliao Basin at $R_o = 0.9\%$. The simulation time for NPT ensemble is 500 ps. Then the simulations are carried out at an NVT ensemble for 1 ns to enable the model to reach the thermodynamic equilibrium. A fixed time step of 1 fs was used, and data was collected every 5 ps,²⁷ the full-precision trajectory was recorded to get the density profiles of oil mixture in the model, and the results were analyzed in the next part.

3. RESULTS AND DISCUSSION

3.1. Volume and Density of Adsorption Oil Phase

To gain insight into the adsorption behavior of eight-component oil mixture molecules confined in the carbonaceous and silica slit-shaped nanopore, local density distributions and configurations of different components after equilibration were collected for oil mixture within 7.92 nm and 8.57 nm slits at 356 K, 18 MPa (Fig. 3). We photoed the last frame of equilibrium model and computed the continuous mass density profile normal to the graphene and silica surface at every $\Delta z = 0.07$ nm interval, which is much smaller than the molecule diameter. Figures 3(b) and (d) shows that the oil mixture molecules are not uniformly distributed throughout the pore, even though the density is symmetrical about the center line ($z = 0$) of two solid walls. Owing to the strong intermolecular affinities between the sheets and the alkanes, intense oscillations of the mass density are present in the vicinity of the interface, and the magnitude is gradually attenuated with increasing

distance from the silica and carbonaceous surface. In the bulk region, computed mass density remains almost constant. The first density peak adjacent to the silica wall is 1.091 g/cm^3 , which is approximately 0.45 time greater than that of the bulk fluid; and the first density peak adjacent to the graphite wall is 2.515 g/cm^3 , which is approximately 2 times greater than that of the bulk fluid; hence, it is reasonable to believe that this layer is in a solid-like state,^{35,36} and indicate that adsorption capacity of mineral is smaller than the organic matter. Away from the near-wall region, the solid-liquid interaction contributes a continuously diminished influence on the mass density, thus leading to a lower density peak of 0.848 g/cm^3 in silica model and 1.286 g/cm^3 in graphite model. The solid walls exert no force on molecules located in the cutoff range of silica and graphite; therefore, the physical properties of the bulk fluid show no strong fluctuations.

With the objective of a more precise estimation of the recoverable oil-in-place, the volume occupied by the adsorption phase, which exists in a solid-like or solid state, must be determined and deducted from the total pore space. The mass density profiles of oil mixture in silica and graphite models (Figs. 3(b) and (d)) reveal that the adsorption region, defined as the section in which their local density deviates from the bulk value,^{37–39} could be considered to contain four molecular layers, indicating multi-layer adsorption of oil mixture molecules on the surface of silica and carbonaceous sheets. The solvation forces between *n*-alkanes and mica surfaces, measured by Christenson et al.,⁴⁰ showed a decaying oscillatory behavior, and the spacing (0.40–0.50 nm) was approximately equal to the width of alkane molecules while independent of the chain length (1.35 nm for *n*-octane). Our results for the thickness of a single layer, ~ 0.44 nm in the silica model and ~ 0.42 nm in the graphite model, determined by measuring the distance between two adjacent crests of the mass density profile (Fig. 3), is in good agreement with their experimental results. Figure 3 also shows that the fluctuation of mass density extends 1.76 nm and 1.68 nm, respectively in the silica model and graphite model, suggesting that, under this condition, the adsorption phase volume on the mineral surface within an 8.57 nm slit is 41.1%, and 42.4% on the organic surface within a 7.92 nm slit. In addition, the adsorption phase mass rate can be calculated from the density and the volume (Eq. (1)). The adsorption phase mass rate in the mineral slit is 42.7%, and 43.1% in the organic slit. What needs illustrating is that these rates can only be used in 8 nm slit.

$$\begin{aligned}
 R_{\text{adsorption}} &= \frac{m_{\text{adsorption}}}{m_{\text{adsorption}} + m_{\text{bulk}}} \cdot 100 \\
 &= \frac{\int_{L_1}^{L_2} \rho_{\text{adsorption}} \cdot L_{\text{adsorption}} \cdot S_{\text{model}}}{\int_{L_1}^{L_2} \rho_{\text{adsorption}} \cdot L_{\text{adsorption}} \cdot S_{\text{model}} + \int_{L_2}^{L_3} \rho_{\text{bulk}} \cdot S_{\text{model}}} \cdot 100 \quad (1)
 \end{aligned}$$

$R_{\text{adsorption}}$ is total adsorption mass rate, %; $m_{\text{adsorption}}$ is adsorption mass, mg; m_{bulk} is bulk mass, mg; $\rho_{\text{adsorption}}$ is

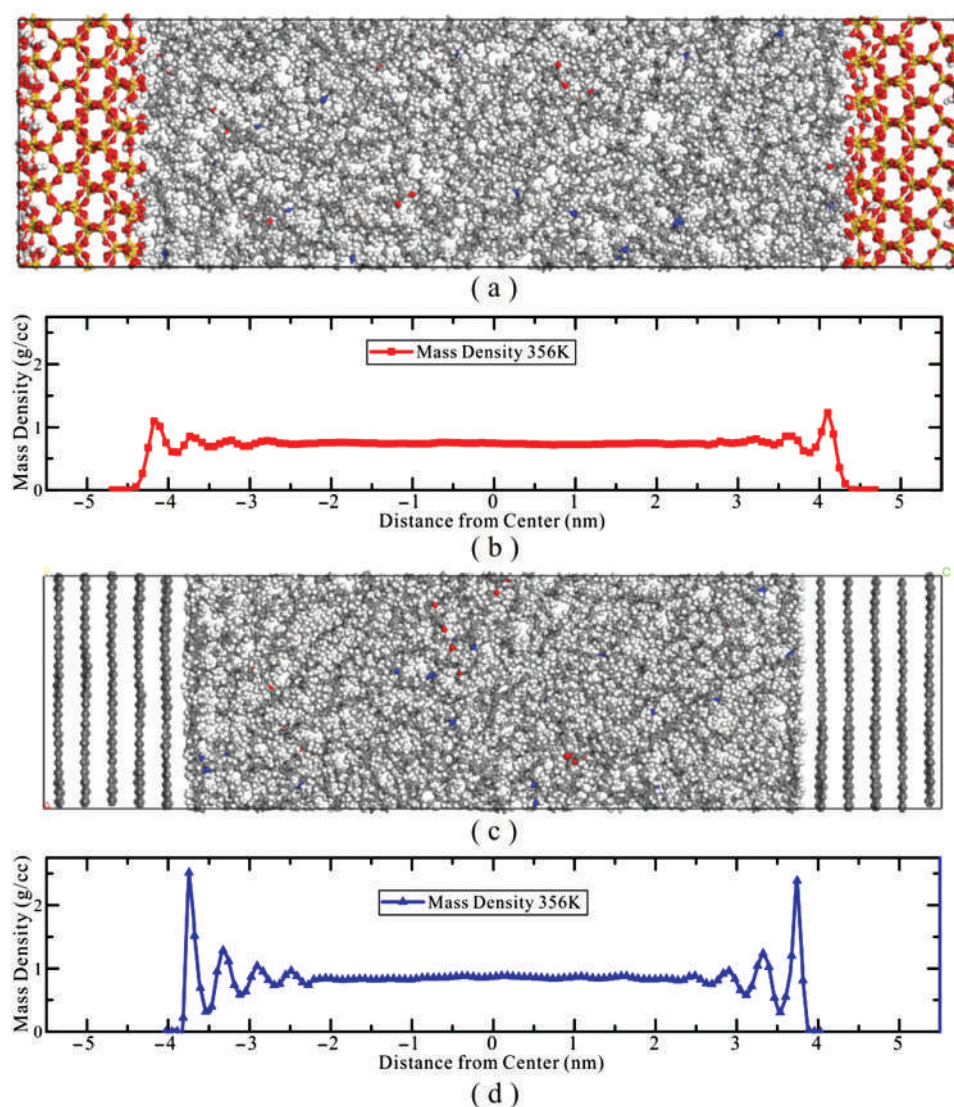


Figure 3. (a) Snapshot (front view) showing the adsorption of oil mixture in a 8.57 nm silica slit (356 K). (b) Mass density profiles for oil mixture in a 8.57 nm silica slit (356 K). (c) Snapshot (front view) showing the adsorption of oil mixture in a 7.92 nm carbonaceous slit (356 K). (d) Mass density profiles for oil mixture in a 7.92 nm carbonaceous slit (356 K).

the density of oil mixture in the adsorption region, g/cm^3 ; ρ_{bluk} is the density of oil mixture in the bulk region, g/cm^3 ; $L_{\text{adsorption}}$ is the length of total adsorption layers, nm; L_{bulk} is the length of bulk, nm; A_{model} is area of the simulation model, nm^2 ; L_1 is the beginning of the density profile, nm; L_2 is the end of the adsorption layers, nm; L_3 is half of the total length of the simulation model, nm. ($\rho_{\text{adsorption}}$, ρ_{bluk} , L_1 and L_2 can be read from the mass density profiles of oil mixture).

To properly account for the effect of oil mixture adsorption on the shale recoverable oil-in-place calculation, the adsorption capacity per unit area ($C_{\text{adsorption-a}}$, mg/m^2) should be used. It is governed by the adsorption mass ($m_{\text{adsorption}}$, mg) and the area of the simulation model (A_{model} , m^2) (Eq. (2)). The $C_{\text{adsorption}}$ of silica and graphite is respectively $1.126 \text{ mg}/\text{m}^2$ and $1.369 \text{ mg}/\text{m}^2$. This conclusion does not seem to agree with the geological knowledge

which shows the adsorption capacity of organic matter is 6.5~15 times bigger than that of shale.⁴¹ But it should be noticed that the unit used in geology is adsorption capacity per unit mass. There is a significant difference between specific surface area (m^2/g) of organic matter and that of shale. The specific surface area of organic matter is 5.66~11.7 times bigger than that of shale.⁴² We can simply put graphene as organic matter, quartz as shale. And if $C_{\text{adsorption}}$ of silica and graphite is multiplied by the specific surface area of shale and organic matter, the result is in accordance with the actual geological conditions.

$$C_{\text{adsorption-a}} = \frac{m_{\text{adsorption}}}{A_{\text{model}}} = \frac{\int_{L_2}^{L_1} \rho_{\text{adsorption}} \cdot L_{\text{adsorption}} \cdot A_{\text{model}}}{A_{\text{model}}} \quad (2)$$

The unrecoverable fraction F_{uc} is governed by the adsorption capacity per unit mass ($C_{\text{adsorption-m}}$, mg/g), the oil content parameter (S_1 , mg/g, the oil mass for 1 g of organic-rich shale) and the specific surface of pores which contain oil (A_{oil} , m²/g) (Eq. (3)).

$$F_{uc} = \frac{C_{\text{adsorption-m}}}{S_1} = \frac{C_{\text{adsorption-a}} \cdot A_{\text{oil}}}{S_1} \quad (3)$$

where,

$$A_{\text{oil}} = A_{\text{shale}} \cdot Z_{\text{oil}}/100 \quad (4)$$

A_{shale} is the specific surface of shale, m²/g; Z_{oil} is the rate of pores which contain oil, %.

The mass of unrecoverable shale oil resource (Q_{uc} , 10⁴ t) can be calculated as followed Eq. (5):

$$Q_{uc} = 10^{-1} \cdot A_{\text{shale}} \cdot H_{\text{shale}} \cdot \rho_{\text{shale}} \cdot S_1 \cdot F_{uc} \quad (5)$$

A_{shale} is the area of shale, km²; H_{shale} is the thickness of shale, m; ρ_{shale} is density of shale, g/cm³.

3.2. Comparison of Multiple Components Adsorption Characters on the Silica and Graphite Surface

Next we will discuss adsorption density and character of each component in the eight-component oil mixture of CH₄, C₂H₆, *n*-C₄H₁₀, *n*-C₈H₁₈, *n*-C₁₈H₃₈, C₁₀H₈, C₁₄H₃₁N, and C₁₈H₃₆O₂ on the silica and graphite surface. The density profile of CH₄, C₂H₆ and *n*-C₄H₁₀ shows one major adsorption layers in the near-wall region of silica surface (Fig. 4(a)), and the peak values are much higher than that of bulk (Fig. 4(b)). And the mean density of the first adsorption layer for CH₄, C₂H₆, and *n*-C₄H₁₀ is approximately 0.1 g/cm³, which is about 3 times larger than the

value of the bulk-fluid region (0.024 g/cm³) (Fig. 4(c)). The thickness of each monolayer, measured as the horizontal distance between two similar points on the damping curve, is also 0.42 nm, by which the discrete mass density profile is determined. In contrast to graphite, the density profile of CH₄, C₂H₆, and *n*-C₄H₁₀ shows four distinct adsorption layers in the near-wall region (Figs. 4(d and e)), this phenomenon is not like the one component CH₄ adsorption character on the mineral surface which has one major adsorption layer,⁴³ due to the exists of other oil components. The gas molecules are not only adsorption by the mineral surface, but also dissolved in the oil mixture. The mean density of the first adsorption layer on the graphite surface is about 0.0523 g/cm³, which is about 0.7464 time larger than the value of the bulk-fluid region (0.030 g/cm³) (Fig. 4(f)). Not only the mean density of the first adsorption layer of CH₄, C₂H₆, and *n*-C₄H₁₀ on the graphite surface is half of that on silica surface, but also the total adsorption mass rate on the graphite is smaller than that on silica surface (respectively 50.197% and 56.677%). This is mainly because there are many defects on the silica surface and the graphite is flat. This makes more adsorption sites exist on the silica surface than the graphite surface. The adsorption density and character of light hydrocarbon (*n*-C₈H₁₈) and heavy hydrocarbon (*n*-C₁₈H₃₈) on the silica and graphite surface are also shown in Figures 5 and 6. The adsorption density of *n*-C₈H₁₈ on the silica surface has the same tide with that of CH₄, C₂H₆, and *n*-C₄H₁₀ on the silica surface, and it also shows one major adsorption layer (Figs. 5(a and b)). And the mean density of the first adsorption layer for *n*-C₈H₁₈ is approximately 0.242 g/cm³, which is about 0.17 time larger than the value of the bulk-fluid region

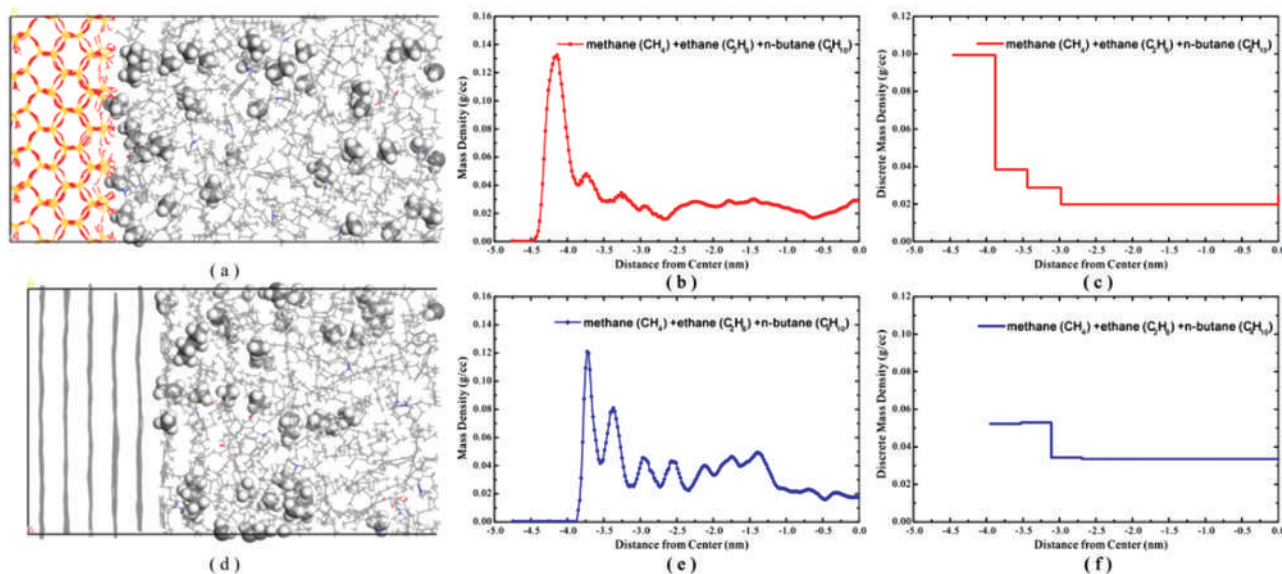


Figure 4. (a) Snapshot (left part) showing the adsorption of gas hydrocarbon (methane (CH₄) + ethane (C₂H₆) + *n*-butane (C₄H₁₀)) in a 8.57 nm silica slit (356 K). (b) Mass density profiles in silica slit. (c) Mean mass density profiles in silica slit. (d) Snapshot (left part) showing the adsorption of gas hydrocarbon in a 7.92 nm graphite slit (356 K). (e) Mass density profiles in graphite slit. (f) Mean mass density profiles in graphite slit.

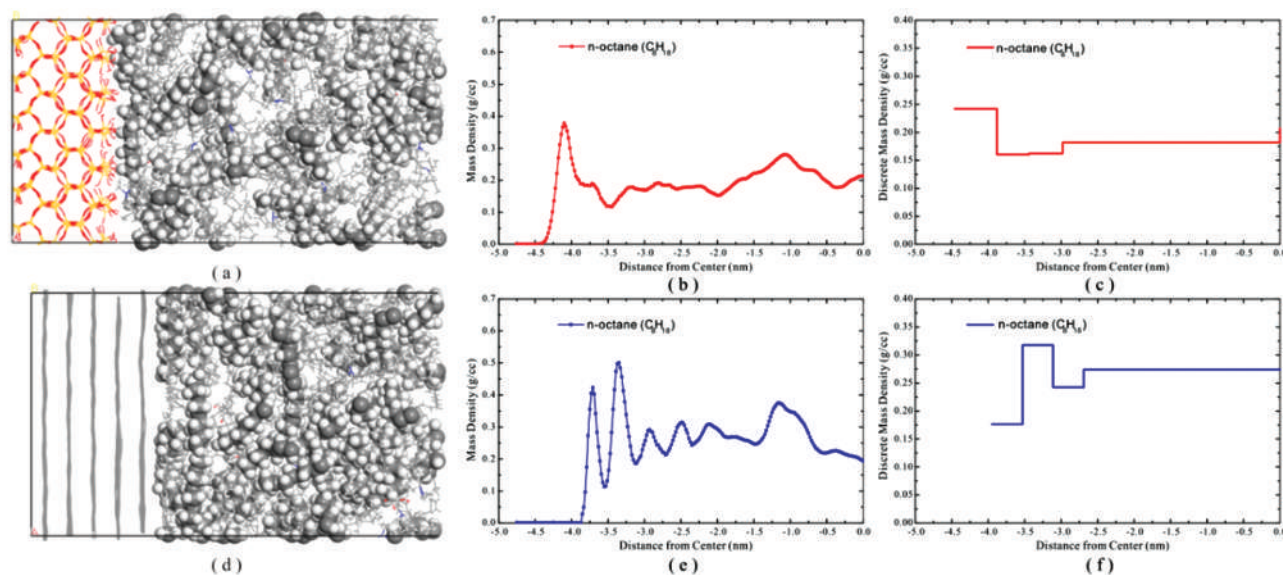


Figure 5. (a) Snapshot (left part) showing the adsorption of *n*-octane (C_8H_{18}) in a 8.57 nm silica slit (356 K). (b) Mass density profiles in silica slit. (c) Mean mass density profiles in silica slit. (d) Snapshot (left part) showing the adsorption of *n*-octane in a 7.92 nm graphite slit (356 K). (e) Mass density profiles in graphite slit. (f) Mean mass density profiles in graphite slit.

(0.207 g/cm^3) (Fig. 5(c)). The density profile of *n*- C_8H_{18} on the graphite has shown four distinct adsorption layers as well as CH_4 , C_2H_6 , and *n*- C_4H_{10} on the graphite surface (Figs. 5(d and e)), but the mean density of the first adsorption layer is smaller than the second adsorption layer (the first adsorption layer: 0.176 cm^3 ; the second adsorption layer: 0.318 cm^3 ; the bulk: 0.272 cm^3) (Fig. 5(f)). Additionally, the density profile of *n*- C_8H_{18} indicates that there are four distinct adsorption layers both on the silica and graphite surface and the first adsorption layer *n*- $C_{18}H_{38}$ is much less than that of the second, the third or the fourth

adsorption layer. The second, third and fourth adsorption layers of the oil mixture on the silica surface are mainly caused by *n*- $C_{18}H_{38}$ (Fig. 6).

The aromatic hydrocarbon (naphthalene) which accounts for only 10% in the oil mixture is adsorption the highest rate in the first adsorption layer, especially on the surface of the graphite (Fig. 7). The naphthalene is adsorption in the first layer on the graphite surface as a flat structure; in addition, it is adsorbed as a stacked structure on the silica surface because of the rough structure and the defects. The density profile of naphthalene shows only

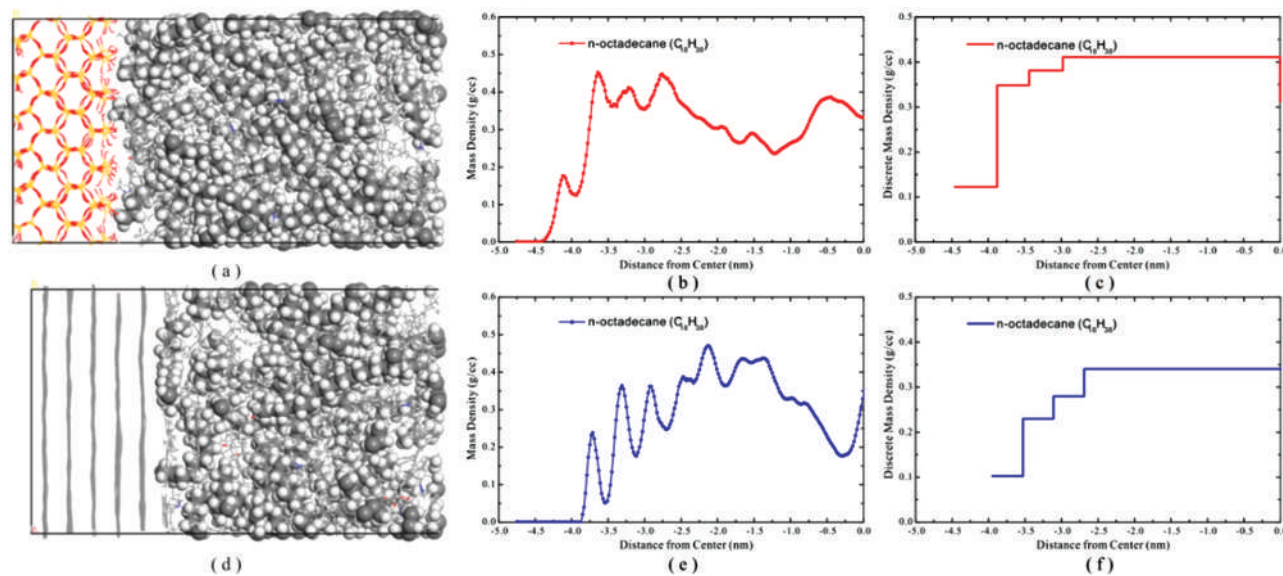


Figure 6. (a) Snapshot (left part) showing the adsorption of *n*-octadecane ($C_{18}H_{38}$) in a 8.57 nm silica slit (356 K). (b) Mass density profiles in silica slit. (c) Mean mass density profiles in silica slit. (d) Snapshot (left part) showing the adsorption of *n*-octadecane in a 7.92 nm graphite slit (356 K). (e) Mass density profiles in graphite slit. (f) Mean mass density profiles in graphite slit.

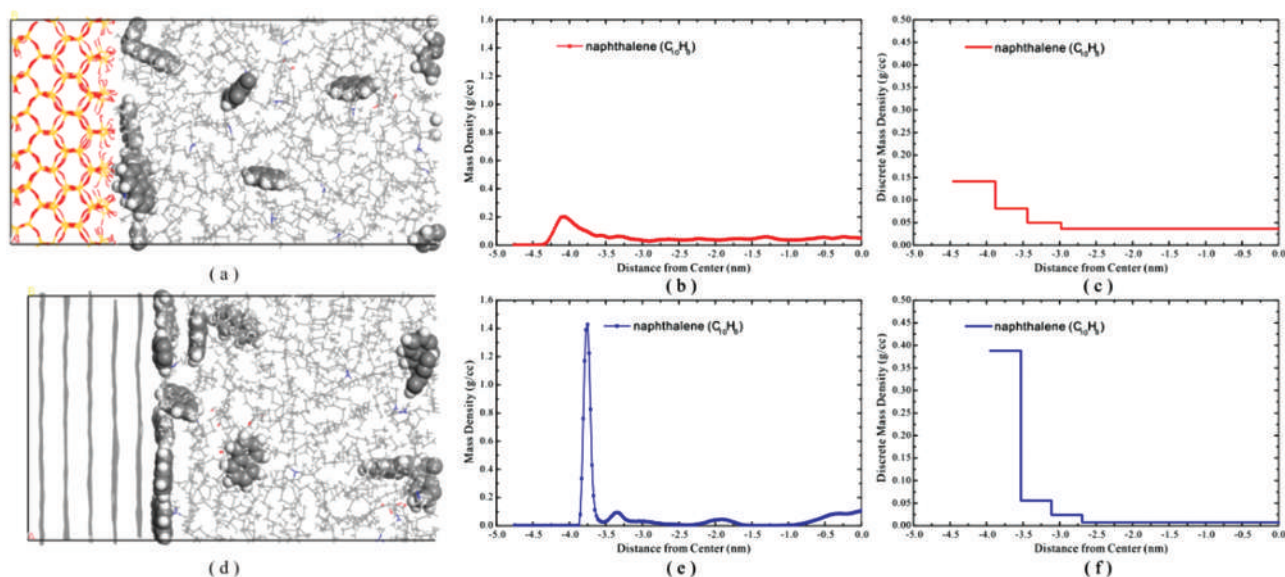


Figure 7. (a) Snapshot (left part) showing the adsorption of naphthalene ($C_{10}H_8$) in a 8.57 nm silica slit (356 K). (b) Mass density profiles in silica slit. (c) Mean mass density profiles in silica slit. (d) Snapshot (left part) showing the adsorption of naphthalene in a 7.92 nm graphite slit (356 K). (e) Mass density profiles in graphite slit. (f) Mean mass density profiles in graphite slit.

one adsorption layer on both silica and graphite surface, and the peak values are 0.202 g/cm^3 and 1.792 g/cm^3 respectively. And the mean density of the first layer is 0.388 g/cm^3 which is much higher than that on the silica surface (0.142 g/cm^3), additionally, the bulk density in the graphite is 0.032 g/cm^3 which is lower than that on the silica surface (0.046 g/cm^3). This indicates the naphthalene adsorption capability of graphite is higher than the silica and the interaction between the naphthalene and graphite is stronger than silica.

Density profiles for the adsorptions of the polar compounds (*N,N*-dimethyldodecylamine ($C_{12}H_{25}N(CH_3)_2$) and octadecanoic acid ($CH_3(CH_2)_{16}COOH$) are also studied. In Figures 8(a)–(f), only one *N,N*-dimethyldodecylamine molecule is adsorbed as an almost parallel orientation to the silica surface like a zigzag arrangement with a certain angle because of the rough surface and the majority of the molecules are amorphous and disordered in the bulk region. The *N,N*-dimethyldodecylamine molecules are also distributed in parallel to the surface and

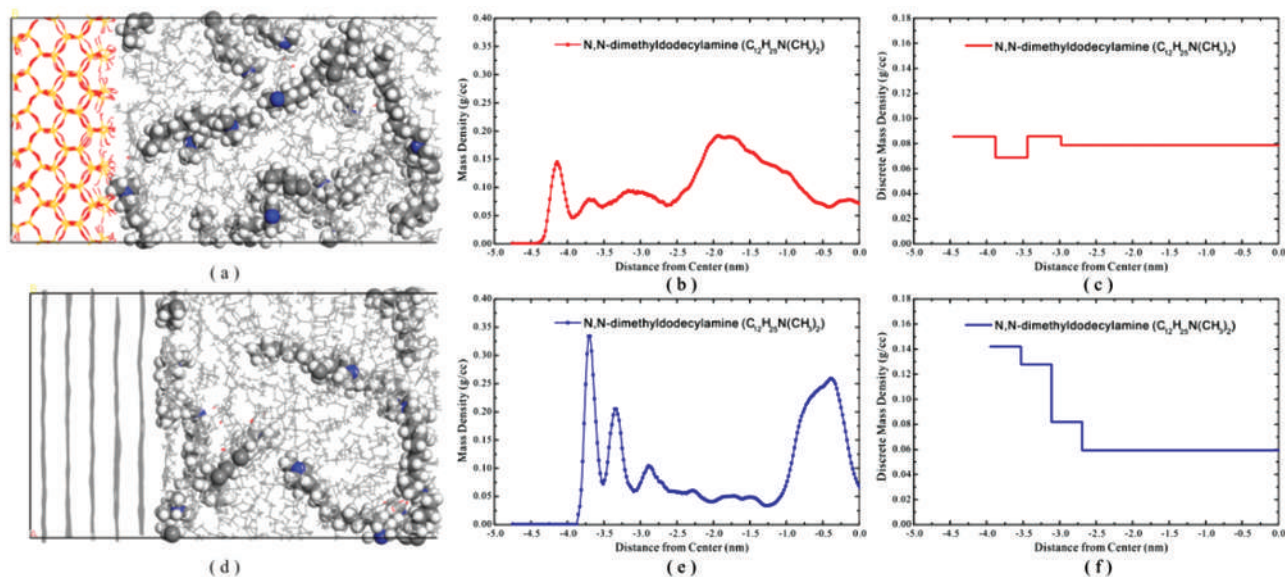


Figure 8. (a) Snapshot (left part) showing the adsorption of *N,N*-dimethyldodecylamine ($C_{12}H_{25}N(CH_3)_2$) in a 8.57 nm silica slit (356 K). (b) Mass density profiles in silica slit. (c) Mean mass density profiles in silica slit. (d) Snapshot (left part) showing the adsorption of *N,N*-dimethyldodecylamine in a 7.92 nm graphite slit (356 K). (e) Mass density profiles in graphite slit. (f) Mean mass density profiles in graphite slit.

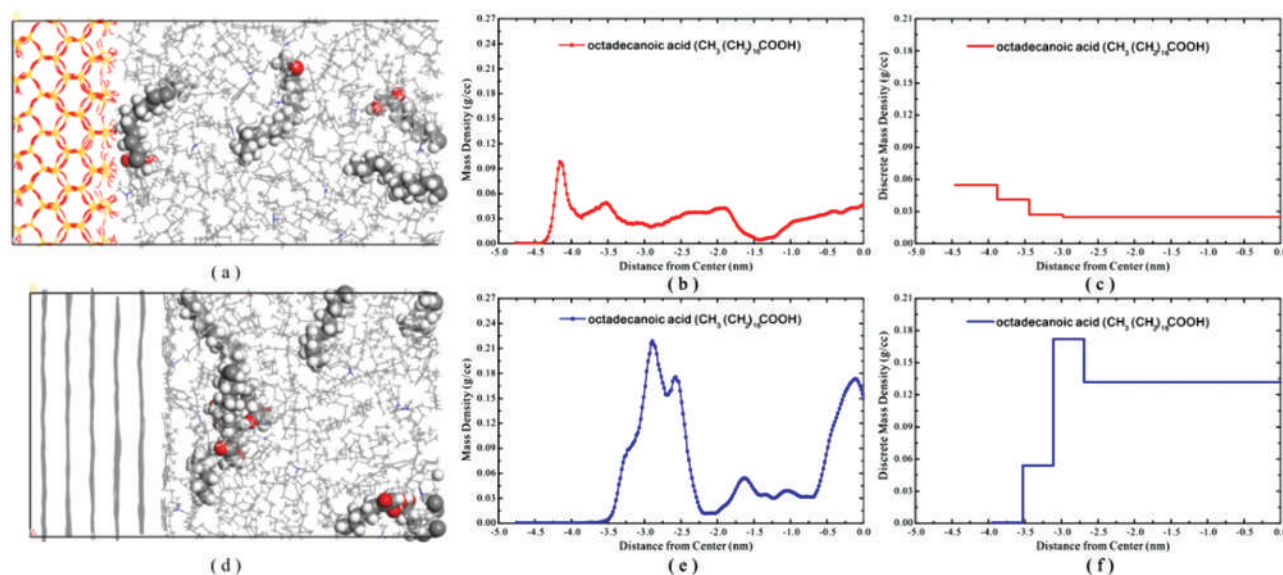


Figure 9. (a) Snapshot (left part) showing the adsorption of octadecanoic acid ($\text{CH}_3(\text{CH}_2)_{16}\text{COOH}$) in a 8.57 nm silica slit (356 K). (b) Mass density profiles in silica slit. (c) Mean mass density profiles in silica slit. (d) Snapshot (left part) showing the adsorption of octadecanoic acid in a 7.92 nm graphite slit (356 K). (e) Mass density profiles in graphite slit. (f) Mean mass density profiles in graphite slit.

the molecules in the bulk region are mainly concentrated in the middle part of the slit. From the density profiles we can see there is mainly one adsorption layer on the silica surface, the density peak of the second and third layer is only half of the first layer. In addition, three adsorption layers are obviously distributed on the graphite surface and the first layer's density peak is 1.333 times higher than that on silica surface (0.35 g/cm^3 and 0.15 g/cm^3 respectively). The mean density of the first layer on the silica is 0.825 g/cm^3 , which is about half of that on graphite surface (0.145 g/cm^3), and the total adsorption mass is also much less. Additionally, the adsorption character in the silica model is not like the tide in the graphite model which decreases with the length from surface. In Figures 9(a)–(f), the head of the octadecanoic acid molecule adsorbs on the silica surface due to the electrostatic interaction between the octadecanoic acid molecule and silica surface. The charges of H atoms of hydroxyl group on the silica surface are $0.250 e$ and the O atoms of carbonyl group in the octadecanoic acid molecule are $-0.419 e$. This interaction is bigger than that on graphite surface caused by Van der Waals force. And there is no octadecanoic acid molecule in the region closest to the graphite surface. From the density profile and the mean density profile we can clearly see that octadecanoic acid molecules are mainly distributed in the first layer on the silica surface, and in the third layer on the graphite surface. Additionally, the total adsorption mass in the graphite model is bigger than that in the silica model.

After comparing the adsorption character and density profile of eight components in the oil mixture, we can conclude that all the eight components expect $n\text{-C}_{18}\text{H}_{38}$ are dominantly with one single adsorption layer in the silica

surface, the second, third, and the fourth adsorption layers are not obvious. Additionally, $n\text{-C}_{18}\text{H}_{38}$ has four adsorption layer, and the adsorption mass rises with the numbers of layers. This phenomenon is not like the adsorption character of single component of which the adsorption mass decreases with the numbers of layers. CH_4 , C_2H_6 , $n\text{-C}_4\text{H}_{10}$, $n\text{-C}_8\text{H}_{18}$, $\text{C}_{14}\text{H}_{31}\text{N}$ have four adsorption layers and C_{10}H_8 are dominantly with one single adsorption layer of which adsorption density peak is much higher than other components. $\text{CH}_3(\text{CH}_2)_{16}\text{COOH}$ and $n\text{-C}_{18}\text{H}_{38}$ have the same adsorption character with $n\text{-C}_{18}\text{H}_{38}$ on silica surface; and no $\text{CH}_3(\text{CH}_2)_{16}\text{COOH}$ appears in the first adsorption layer. The silica surface adsorbs more CH_4 , C_2H_6 , $n\text{-C}_4\text{H}_{10}$, and $\text{CH}_3(\text{CH}_2)_{16}\text{COOH}$ than graphite because of the shape of alkane gas molecules and the negative charge of $\text{CH}_3(\text{CH}_2)_{16}\text{COOH}$. Graphite adsorbs more C_{10}H_8 than silica; because graphite and C_{10}H_8 have the conjugated π bond and the shape of C_{10}H_8 is not suitable to rough surface of silica. Both silica and graphite have the same adsorption character of $\text{C}_{18}\text{H}_{38}$; and the total adsorption mass on silica surface is a little bigger than that on graphite. Multiple component adsorption characters on silica and graphite surface indicate that mineral and organic matter have different adsorption capabilities of different component. Additionally, the oil mixture adsorbed on silica surface is lighter than that on graphite.

3.3. Effect of Temperature on Oil Mixture Adsorption

The adsorption of oil mixture in 7.92 nm organic slit and SiO_2 slit were computed at temperatures of 356 K and 388 K; oil mixture and compositions density distributions are shown in Figure 10. As with the aforementioned

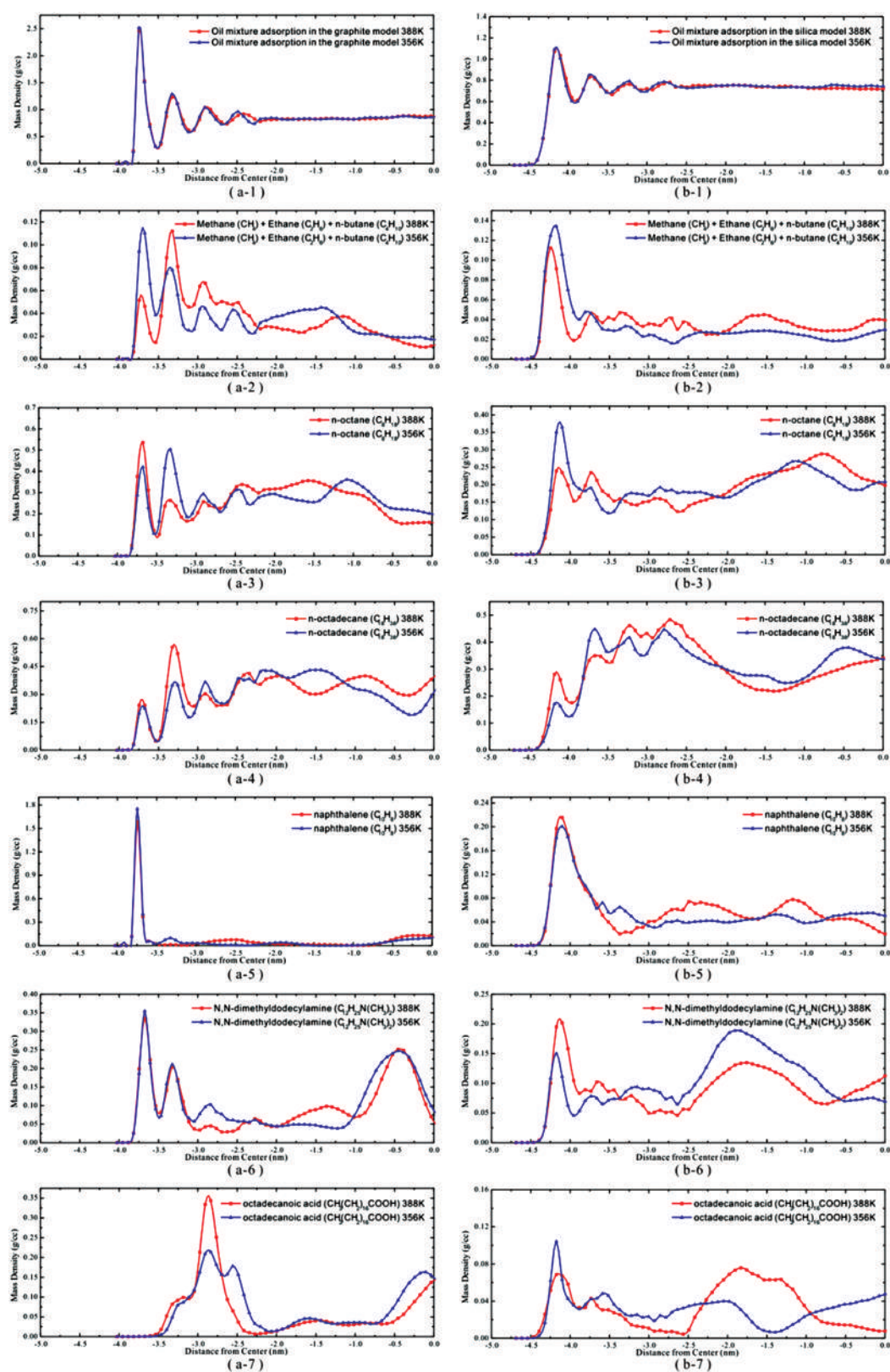


Figure 10. Effect of temperature on the left panels and mass density profiles for oil mixture and different components in carbonaceous slits (a1–a7) and silica slits (b1–b7). (a1) Mass density profiles for oil mixture in carbonaceous slits. (a2) Mass density profiles for gas hydrocarbon in carbonaceous slits. (a3) *n*-octane. (a4) *n*-octadecane. (a5) naphthalene. (a6) *N,N*-dimethyldodecylamine. (a7) octadecanoic acid. (b1) Mass density profiles for oil mixture in silica slits. (b2) Mass density profiles for gas hydrocarbon in silica slits. (b3) *n*-octane. (b4) *n*-octadecane. (b5) naphthalene. (b6) *N,N*-dimethyldodecylamine. (b7) octadecanoic acid. Only the left-half parts of the symmetric slits are shown.

results, there are four adsorption layers on the pore surface under different temperatures (Figs. 10(a-1 and b-1)). Differing from expected, both organic silt and SiO₂ silt indicate that the adsorption layer density changing little with increasing temperature (Figs. 10(a-1 and b-1)). Moreover, in the same adsorption model, various compositions show different changes with the increase of temperature (Figs. 10(a-2~a-7)), and the same component indicate different tendencies with different silts (Figs. 10(a-2) and (b-2); (a-3) and (b-3); (a-4) and (b-4); (a-5) and (b-5); (a-6) and (b-6); (a-7) and (b-7)). In the organic silt, density of oil mixture decreases with the increase of temperature in the last two adsorption layers, and increases in the last two layers; meanwhile, in the SiO₂ silt, density of oil mixture decreases with the increase of temperature in the last three adsorption layers, and increases in the first layer (Figs. 10(a-1 and b-1)). In the organic silt and SiO₂ silt, densities of methane, ethane, and *n*-butane both decrease with the increase of temperature in the first adsorption layer; meanwhile, increase with the increase of temperature in the last three adsorption layers (Figs. 10(a-2 and b-2)). In the organic silt density of *n*-octane increases with the increasing temperature in the first and fourth layers, and decreases in the second and third layers (Fig. 10(a-3)). In the SiO₂ silt density of *n*-octane increases with the increasing temperature in the second layer, and decreases in the other three layers (Fig. 10(b-3)). In the organic silt density of *n*-octadecane decreases with the increasing temperature in the third layer, and increases in the other three layers (Fig. 10(a-4)); meanwhile, in the SiO₂ silt density of *n*-octadecane decreases with the increasing temperature in the second layer, and increases in the other three layers (Fig. 10(b-4)). In the organic silt density of naphthalene decreases with the increasing temperature in the first two adsorption layers, and increases in the last two layers (Fig. 10(a-5)); meanwhile, in the SiO₂ silt density of naphthalene decreases with the increasing temperature in the second and third adsorption layers, and increases in the other two layers (Fig. 10(b-3)). In the organic silt density of *N,N*-dimethyldodecylamine decreases with the increasing temperature almost all the adsorption layers (Fig. 10(a-6)); meanwhile, in the SiO₂ silt density of *N,N*-dimethyldodecylamine decreases with the increasing temperature in the last two layers, and increases in the first two layers (Fig. 10(b-6)). In the organic silt density of octadecanoic acid decreases with the increasing temperature in the last layer, and increases in the first three layers (Fig. 10(a-7)); meanwhile, in the SiO₂ silt density of octadecanoic acid decreases with the increasing temperature almost all the adsorption layers (Fig. 10(b-7)).

Results of molecular modeling of oil mixture adsorption in different temperature indicate that the impact of temperature on the oil mixture adsorption is different from single component adsorption model. In the single component model, density decreases with the growth of temperature in all the four adsorption layers; nevertheless, in the

multiple components model, densities of various components changes differ from each other and show different from four adsorption layers. For example, changing rate of bulk phase is the more than adsorption phase in methane, ethane, and *n*-butane adsorption graphite and SiO₂ model; rate of change of the third layer is more than other three layers in adsorption layers in organic silt and rate of change of the second layer is more than other three layers in adsorption layers in SiO₂ silt. What's more, change rates of other components are different either. Additionally, density change rate of the same component (all components except *n*-octane) influenced by temperature in graphite silt and SiO₂ silt is similar, though the rates in each adsorption layer are different. That is to say density change rate of one component in adsorption and bulk phases is more likely related to the property and content, other than the solid silt.

4. CONCLUSION

On the basis of adsorption characteristics of oil mixture on the graphite surface (oil-wet) and the hydroxyl silica surface (water-wet), we study the total adsorption phase thickness in the slits and the characters of each component. We reached the following conclusions:

- (1) Under reservoir conditions, there are four adsorption layers of oil mixture on silica and graphite surface, and the thickness of each layer is 0.44 nm in the silica model and 0.42 nm in the graphite model. In particular, the adsorption phase volume on the mineral surface within a 8.57 nm slit is 41.1%, and 42.4% on the organic surface within a 7.92 nm slit. In addition, the adsorption *c* mass in the mineral slit is 42.7%, and 43.1% in the organic slit. The adsorption capacity per unit area of silica and graphite is respectively 1.126 mg/m² and 1.369 mg/m². We can anticipate that adsorption capability per unit mass used in geology is mainly governed by specific surface area.
- (2) The adsorption character of single component in oil mixture depends largely on its property: the adsorption mass of high carbon number alkane increases with the numbers of adsorption layers, of which trend is contrary to that of light carbon numbers alkane; aromatic hydrocarbon has mainly one adsorption layer; the adsorption character of polar compounds depends on their electric charge. Silica surface is more likely to adsorb the light carbon number alkane than graphite because of its rough surface; and compounds with negative charge trend to be adsorbed more on the silica surface than graphite due to the hydroxyls of silica. Graphite adsorbs more C₁₀H₈ than silica, because graphite and C₁₀H₈ have the same conjugated π bond and the shape of C₁₀H₈ is not suitable to rough surface of silica.
- (3) For oil in shale systems, the density of adsorption phase decreases with temperature, and the effect of temperature on the adsorption of macromolecular compounds is greater. Thermal processes may therefore provide us a

potential avenue to improve recoverable oil from shale, especially the heavy oil.

Acknowledgments: This work is supported by the National Natural Science Foundation of China (41572122, 41330313, 41672116), National Science and Technology Major Project (2016ZX05004-001, 2016ZX05007-003), National Basic Research Program of China (973 Program) (2014-CB239005), Graduate Innovation Fund of China University of Petroleum (YCXJ2016004).

References and Notes

1. K. A. Bowker, *AAPG Bulletin* 91, 523 (2007).
2. D. M. Jarvie, R. J. Hill, T. E. Ruble, and R. M. Pollastro, *AAPG Bulletin* 91, 475 (2007).
3. D. J. K. Ross and R. M. Bustin, *AAPG Bulletin* 92, 87 (2008).
4. N. Z. Cai, D. Z. Dong, S. J. Wang, J. Z. Li, X. J. Li, Y. Wang, D. H. Li, and K. M. Cheng, *Petroleum Exploration and Development* 37, 641 (2010).
5. H. Brian and H. M. Schulz, *Marine and Petroleum Geology* 31, 1 (2012).
6. T. J. Kinley, L. W. Cook, J. A. Breyer, D. M. Jarvie, and A. B. Busbey, *AAPG Bulletin* 92, 967 (2008).
7. P. P. Kuhn, R. di. Primio, R. Hill, J. R. Lawrence, and B. Horsfield, *AAPG Bulletin* 96, 1867 (2012).
8. M. A. Kirschbaum and T. J. Mercier, *AAPG Bulletin* 97, 899 (2013).
9. EIA. Shale in the United States. U.S. (https://www.eia.gov/energy_in_brief/article/shale_in_the_united_states.cfm) (2016).
10. L. Doman, Energy Information Administration, U.S. (<http://www.eia.gov/todayinenergy/detail.cfm?id=26352>) (2016).
11. EIA, Outlook for shale gas and tight oil development in the U.S. (<http://www.eia.gov/pressroom/presentations>) (2013).
12. L. Zhang, Y. Bao, J. Li, Z. Li, R. Zhu, and J. Zhang, *Petrol. Explor. Dev.* 41, 703 (2014).
13. C. Zou, Z. Yang, G. Zhang, L. Hou, R. Zhu, S. Tao, X. Yuan, D. Dong, Y. Wang, Q. Guo, L. Wang, H. Bi, D. Li, and N. Wu, *Petrol. Explor. Dev.* 41, 14 (2014).
14. EIA, Technically Recoverable Shale Oil and Shale Gas Resources: An Assessment of 137 Shale Formations in 41 Countries Outside the United States, USA, (<http://www.eia.gov/analysis/studies/worldshalegas/>) (2015).
15. C. Z. Jia, M. Zheng, and Y. F. Zhang, *Acta Petrolei Sinica* 35, 1 (2014).
16. C. N. Zou, G. M. Zhai, G. Y. Zhang, H. J. Wang, G. S. Zhang, J. Z. Li, Z. M. Wang, Z. X. Wen, and F. Ma, *Petroleum Exploration and Development* 42, 1 (2015).
17. P. H. Nelson, *AAPG Bull* 93, 329 (2009).
18. C. Zou, Z. Yang, J. Cui, R. Zhu, L. Hou, S. Tao, X. Yuan, S. Wu, S. Lin, L. Wang, B. Bai, and J. Yao, *Petrol. Explor. Dev.* 40, 14 (2013).
19. X. Tang, J. Zhang, and X. Wang, *Int. J. Coal Geol.* 128, 32 (2014).
20. G. C. McGonigal, R. H. Bernhardt, and D. J. Thomson, *Appl. Phys. Lett.* 57, 28 (1990).
21. M. A. Castro, S. M. Clarke, A. Inaba, C. C. Dong, and R. K. Thomas, *J. Phys. Chem. B* 102, 10528 (1998).
22. B. L. Severson and R. Q. Snurr, *J. Chem. Phys.* 126, 134708 (2007).
23. A. Harrison, R. F. Cracknell, J. Krueger-Venus, and L. Sarkisov, *Adsorption* 20, 427 (2014).
24. R. J. Ambrose, R. C. Hartman, and I. Y. Akkutlu, Society of Petroleum Engineers SPE-141416-MS, Oklahoma City, OK (2011).
25. R. J. Ambrose, R. C. Hartman, M. Diaz-Campos, I. Y. Akkutlu, and C. H. Sondergeld, *SPE J.* 17, 219 (2012).
26. R. C. Hartman, R. J. Ambrose, I. Y. Akkutlu, and C. R. Clarkson, Society of Petroleum Engineers SPE-144097-MS, Woodlands, TX (2011).
27. S. Wang, Q. Feng, F. Javadpour, T. Xia, and Z. Li, *International Journal of Coal Geology* 147, 9 (2015).
28. H. Sun, *J. Phys. Chem. B* 102, 7338 (1998).
29. H. Sun, P. Ren, and J. R. Fried, *Computational and Theoretical Polymer Science* 8, 229 (1998).
30. M. E. Curtis, B. J. Cardott, C. H. Sondergeld, and C. S. Rai, *Int. J. Coal Geol.* 10, 26 (2012).
31. J. J. Li, J. X. Yin, Y. N. Zhang, S. F. Lu, W. M. Wang, J. B. Li, F. W. Chen, and Y. L. Meng, *International Journal of Coal Geology* 152, 83 (2015).
32. M. Wang, S. F. Lu, and H. T. Xue, *Marine and Petroleum Geology* 28, 1714 (2011).
33. Y. Tang, P. D. Jenden, A. S. Nigrini, and S. C. Teerman, *Energy and Fuels* 10, 659 (1996).
34. M. Levitt and S. J. Lifson, *Mol. Biol.* 46, 269 (1969).
35. M. Sha, F. Zhang, G. Wu, H. Fang, C. Wang, S. Chen, Y. Zhang, and J. Hu, *Chem. Phys.* 128, 134504 (2008).
36. S. Wang, Q. Feng, F. Javadpour, T. Xia, and Z. Li, *International Journal of Coal Geology* 147, 9 (2015).
37. D. D. Do and H. D. Do, *Chem. Eng. Sci.* 60, 1977 (2005).
38. B. L. Severson and R. Q. Snurr, *Chem. Phys.* 126, 134708 (2007).
39. M. Sha, F. Zhang, G. Wu, H. Fang, C. Wang, S. Chen, Y. Zhang, and J. Hu, *Chem. Phys.* 128, 134504 (2008).
40. H. K. Christenson, D. W. R. Gruen, R. G. Horn, and J. N. Israelachvili, *Chem. Phys.* 87, 1834 (1987).
41. H. J. Guo, W. L. Jia, P. A. Peng, Y. H. Lei, X. R. Luo, M. Cheng, X. Z. Wang, L. X. Zhang, and C. F. Jiang, *Marine and Petroleum Geology* 57, 509 (2014).
42. T. T. Cao, Z. G. Song, S. B. Wang, X. X. Cao, Y. Li, and J. Xia, *Science China* 45, 139 (2015).
43. Y. Liu and J. Wilcox, *International Journal of Coal Geology* 104, 83 (2012).

Received: 12 March 2016. Accepted: 13 September 2016.